Multispectral Brain Tumor Segmentation based on Histogram Model Adaptation

Jan Rexilius[a], Horst K. Hahn[a], Jan Klein[a],
Markus G. Lentschig[b], and Heinz-Otto Peitgen[a]

[a]MeVis Research, Universitaetsallee, Bremen, Germany;
[b]Center for Magnetic Resonance Imaging, ZKH St.-Juergen-Strasse, Bremen, Germany

ABSTRACT

Brain tumor segmentation and quantification from MR images is a challenging task. The boundary of a tumor and its volume are important parameters that can have direct impact on surgical treatment, radiation therapy, or on quantitative measurements of tumor regression rates. Although a wide range of different methods has already been proposed, a commonly accepted approach is not yet established. Today, the gold standard at many institutions still consists of a manual tumor outlining, which is potentially subjective, and a time consuming and tedious process.

We propose a new method that allows for fast multispectral segmentation of brain tumors. An efficient initialization of the segmentation is obtained using a novel probabilistic intensity model, followed by an iterative refinement of the initial segmentation. A progressive region growing that combines probability and distance information provides a new, flexible tumor segmentation. In order to derive a robust model for brain tumors that can be easily applied to a new dataset, we retain information not on the anatomical, but on the global cross-subject intensity variability. Therefore, a set of multispectral histograms from different patient datasets is registered onto a reference histogram using global affine and non-rigid registration methods. The probability model is then generated from manual expert segmentations that are transferred to the histogram feature domain. A forward and backward transformation of a manual segmentation between histogram and image domain allows for a statistical analysis of the accuracy and robustness of the selected features. Experiments are carried out on patient datasets with different tumor shapes, sizes, locations, and internal texture.

Keywords: tumor segmentation, histogram model, magnetic resonance, risk assessment, treatment planning

1. INTRODUCTION

Brain tumor segmentation is an essential task for treatment planning and quantitative follow-up assessment. Typical multispectral magnetic resonance (MR) image acquisition protocols include a set of different sequences. Common, primary brain tumors such as gliomas have a high variability in appearance, size, location, and structure.[1] They also have a tendency to infiltrate adjacent normal brain tissue, and thus often appear to have no particular margin on an MR scan. This makes treatment even more difficult, and the development of dedicated image analysis tools for the computation of exact boundaries and volumes of the tumor a challenging task. Therfore, the current gold standard for validation today is often a purely visual assessment.

Several computer assisted methods have been proposed for the segmentation and quantification of brain tumors, ranging from manual or user-assisted outlining performed by a medical expert[2] to fully automatic methods.[3] Common approaches include classification methods such as expectation-maximization[4] or fuzzy-connectedness.[5] An atlas-based approach that combines non-ridig registration of a brain template with a k-nearest neighbor classification has been proposed by Kaus et al.[6,7] Another popular type of techniques for tumor segmentation is related to deformable models and level set methods. Therein, an initial curve or surface is propagated through the object based on a number of driving forces.[8–10] Unfortunately, the choice of these forces often constrains the potential tumor shapes to rather blobby structures, which is usually for post-surgical cases not a valid assumption. Today, a widely accepted approach for tumor segmentation is not yet established, and manual outlining the tumor boundaries on each slice is still a standard procedure in many clinical settings.[2]

Further author information: (Send correspondence to: J. Rexilius)
J. Rexilius: email: rexilius@mevis.de, phone: +49-421-218-9561

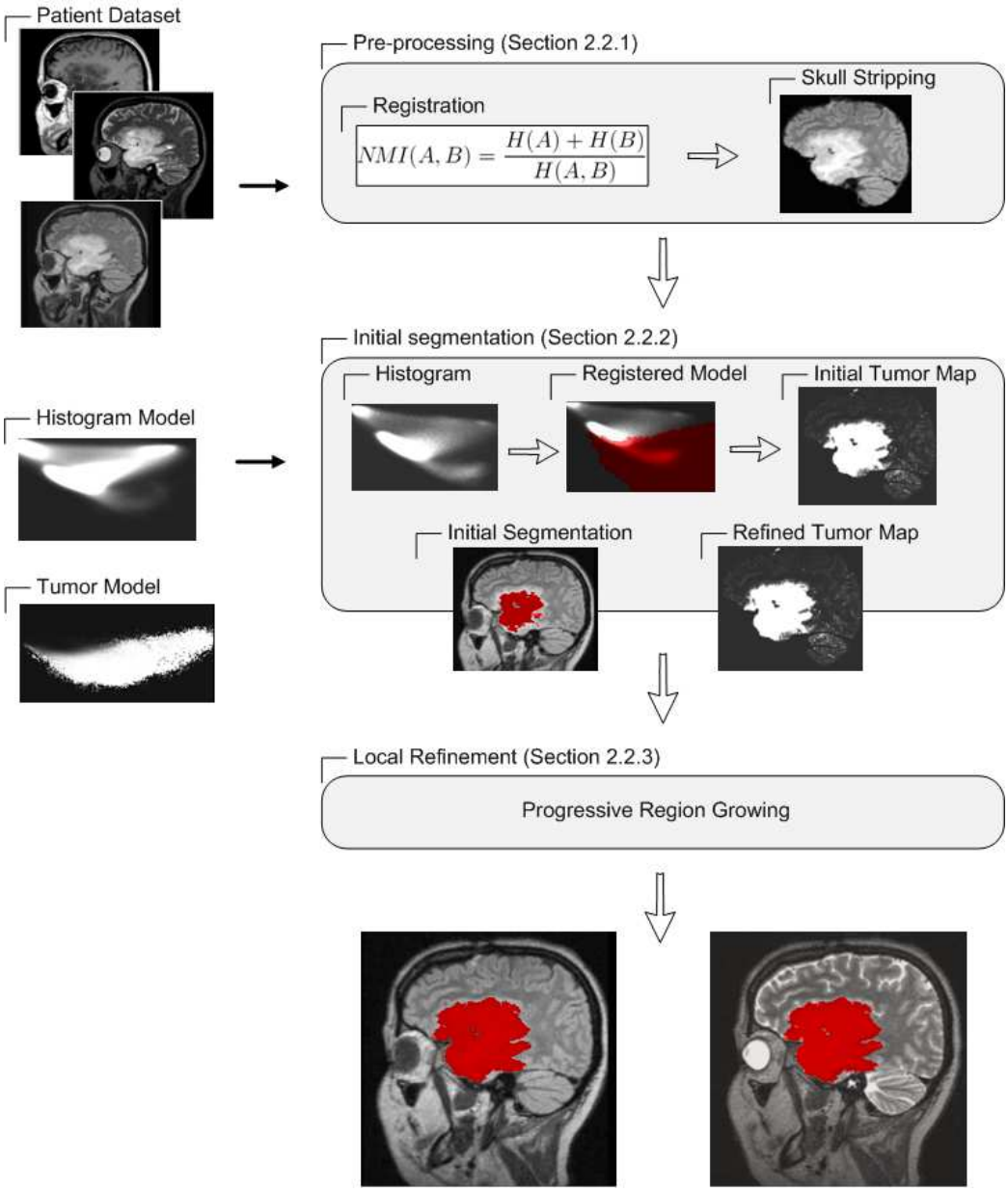

Figure 1. Structure of the proposed segmentation algorithm.

In order to achieve an adequate segmentation, appropriate initializations for each considered tissue class are an important requirement. Commonly applied methods include manual placing of example tissue points[6] or registration of an atlas dataset onto a patient dataset.[11] However, different anatomies as well as different shapes, sizes, and locations between atlas and patient dataset complicate this task, and a precise registration can take a significant amount of time. Furthermore, the employed brain atlas may lead to incorrect initializations, e.g. in case of large deformations due to tumor growth. Especially, information about pathological tissue such as tumor is generally missing in current brain atlases. A common approach for the modelling of tumor tissue is to provide an intensity model, assuming a mixture of density functions. Popovic et al. proposed an a priori tumor intensity model (or *believe map*) for the segmentation of calvarial tumors from CT images.[10] In their work, a mixture of Gaussians generated from a number of training datasets is incorporated into a level set framework.

An empirical intensity model[12] is used for comparison. Recently, Ho et al. proposed a patient specific tumor map computed from the difference between two T1-weighted MR images, with and without contrast agent.[8] A histogram analysis is used to convert the difference image into a probability distribution, assuming a mixture of a Gaussian function and a Poisson distribution. Further extensions of this work are proposed by Prastawa et al.[4] A patient specific extraction of enhancing tumor tissue from this difference image has also been proposed based on fuzzy-connectedness.[5]

The approach presented in this paper aims at introducing a new method for the multispectral brain tumor segmentation. We present an efficient and robust segmentation that can be provided within minutes. Therefore, we perform a fast histogram matching, based on a novel probabilistic model generated in a multispectral histogram feature space, which particularly allows for a fast and robust initial segmentation. This step is then followed by a local refinement based on a progressive region growing. Furthermore, the transformation of manual segmentations between histogram and image domain can provide an analysis of accuracy and robustness of selected features.

2. METHODS

In order to differentiate tumor from other brain tissue classes, multispectral patient datasets are an essential requirement. Our segmentation method consists of two basic steps. In a first step, a probabilistic tumor model is aligned with the patient dataset. The registered model is then used to compute an initial tumor segmentation that is iteratively refined by means of a progressive region growing approach. A general overview of the specific steps is given in Figure 1.

2.1. Model Generation

Various approaches exist to capture a priori information about anatomical structure and function of the brain.[13–15] Probabilistic atlases have become a popular tool, since they offer a framework for the modelling of cross-subject variability. The information stored in the model can then be used to analyse new patient datasets. Furthermore, probabilistic models can be easily extended as the population database increases, which will also lead to a more accurate representation of the variability of the observed structure. However, anatomical models of pathological structures such as tumor tissue are difficult to develop due to their high variability.

In this work, we propose a probabilistic model for brain tumors that retains information not on the anatomical, but on the global cross-subject intensity variability. The resulting feature space is based on multispectral patient datasets $V : \Omega \rightarrow \mathbb{R}^c$ with c channels and signal intensity values $v := v(x)$ at voxel positions x, represented by a multidimensional gray value histogram $H : \mathbb{R}^c \rightarrow \mathbb{R}$. Example histograms are shown in Figure 2. For each patient dataset, a manual segmentation of the tumor region is generated and transferred to this histogram feature space, where the gray values are the only features used to differentiate tumor from other brain tissue. This results in a probability map for tumor tissue intensities with the relative frequency of tumor stored for each feature vector. However, gray value ambiguities in the images can constrain the overall accuracy and robustness, as shown in the result section (cf. Section 3.1).

In advance to the model generation step, motion correction of all available MR sequences as well as a skull stripping are preformed (cf. Section 2.2.1). Therefore, we can assume the same tissue types occurring in each dataset as well as similar histogram shapes. A probabilistic model of empirical tumor variability is then constructed by matching histograms from different patients onto an arbitrarily selected reference histogram. Although histogram matching is a common method in the 1D case,[8,10,11] a multispectral extension is rarely found for medical image segmentation. An unsupervised learning algorithm for multispectral brain segmentation has been proposed by Wismueller et al.[16] Based on a set of feature vectors, e.g. derived from a training dataset, a self-organized deformable model adaptation is used to establish an optimal correspondence between training data and observed data. Another related approach focuses on the automatic adjustment of 2D transfer functions for volume visualization[17] using non-rigid registration. Since we work on a multispectral (2D, 3D) feature space, image registration methods can be adapted here as well, which provides us with a set of very efficient and robust algorithms.

We apply a global affine as well as a local registration to align the considered histogram with the reference dataset. Due to the high variability even with respect to its intensities, the tumor region is cropped from the

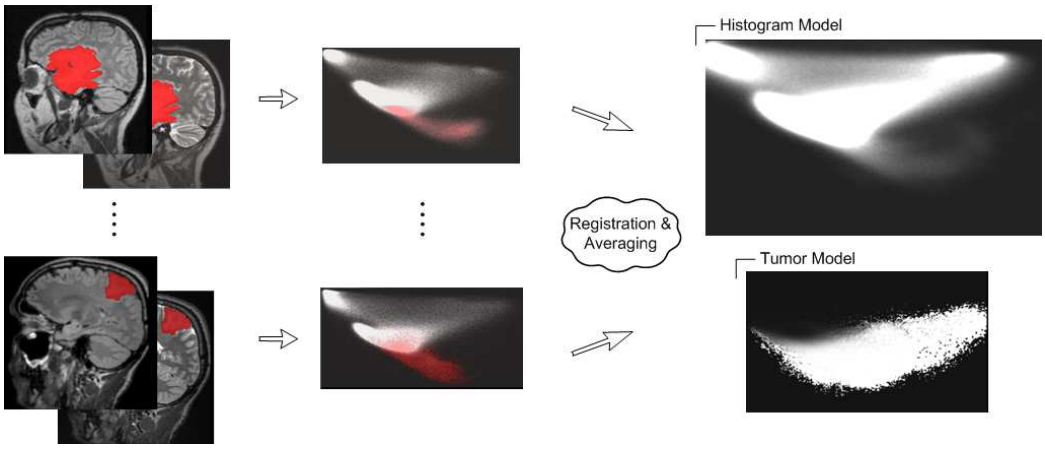

Figure 2. Histogram and tumor model construction.

datasets before registration. The global registration is further regularized, by smoothing the histogram data with a nonlinear diffusion filtering.[18] The subsequent local registration uses a free-form deformation based on B-splines[19] defined on a uniformly spaced control point grid covering the histogram image. In a final step, an average-intensity atlas is generated on the histogram data, including the tumor region (cf. Fig. 2). Furthermore, the deformation fields are applied to the cropped tumor regions. A combination of the registered tumor probability maps then yields an average histogram shape model for tumor plus an average tumor probability map (cf. Fig. 2).

2.2. Segmentation

Our proposed segmentation method combines a general pre-processing step with a new tumor segmentation approach, as shown in Figure 1. First, a global motion correction of all available MR sequences is performed, followed by an extraction of the intracranial cavity (ICC). In a subsequent step, the tumor segmentation is carried out, based on the previously generated probabilistic tumor model (cf. Section 2.1).

2.2.1. Pre-processing

Before identifying the tumor, a number of pre-processing steps have to be performed. In a first step, a compensation for motion artefacts is employed on all available MR sequences (T1 post contrast, T2, FLAIR). We apply an automatic, global affine alignment, using the entropy-based normalized mutual information (NMI)[20] as similarity measure. The T2-weighted images are used as reference for the registration. Then, the brain is extracted, which helps to reduce the overall gray value ambiguity and thus allows for more accurate tissue segmentation. The resulting brain mask can also be used for a subsequent segmentation of other tissue classes such as gray matter, white matter, and cerebrospinal fluid. We apply a marker-based watershed transform to extract the brain, which has shown to be very robust even on low quality images.[21] Although this method does not provide a fully automatic brain segmentation, only limited user interaction is required. Up to seven include markers are placed inside the brain and another five to ten exclude markers are required to separate the brain from other adjacent structures, depending on the patient dataset.

2.2.2. Initial segmentation

After extracting the brain, the intial tumor segmentation is carried out. Therefore, the previously generated histogram atlas is registered onto the multispectral histogram of the current patient dataset. Similar to the model generation step, a global affine transformation followed by a B-spline based non-rigid registration is performed (cf. Section 2.1). The resulting deformation field is used to register the probabilistic tumor model onto the dataset, thus permitting a classification of the patient tumor region. In the next step, the classified histogram is applied to the original image data, which can be considered as transformation from histogram space back into

the image domain. We obtain a tumor probability map $V_p : \Omega \rightarrow \mathbb{R}$ with intensity values $v_p := v_p(x) \in [0, 100]$. The accuracy and robustness of this step can be directly measured as proposed in Section 3.1.

Since the transformation into the image domain will yield classification errors with mis-classified voxels in both the tumor and the non-tumor region, several processing steps are added, resulting in an adequate assessment of the initial tumor mask. First, all voxels with an estimated tumor probability of more than 90% are extracted. In this mask, small holes are filled followed by a connected component operation on a typical 6 neighborhood N_6. All components whose size do not deviate more than 90% from the largest component are included in the tumor mask. This removes isolated, mis-classified speckles and enables a proper segmentation of tumor fractions that are not connected to the largest component, e.g. for data acquired after surgical resection. An exemplary mask resulting from this step is given in Figure 1.

Due to the above-mentioned classification errors, we also update the tumor probability map in addition to the initial tumor mask extraction. To this end, we compute new mean values for tumor and background respectively. The new mean value for tumor μ_t is extracted from the boundary of the current tumor mask. The mean background value μ_{bg} can be estimated directly from the histogram. All tumor probabilities $< 90\%$ are averaged and then further decreased 10%, due to imperfect model to data registration. The new probability is now computed as average over the original value v_p and its scaled fractional distance $d = \frac{<v_p - \mu_{bg}, \mu_t - \mu_{bg}>}{\|\mu_t - \mu_{bg}\|^2} \cdot 100 \in [0, 100]$ between the two mean values, i.e. $v_p = [\, d(v_p) + v_p \,]/2$.

2.2.3. Local refinement of the segmentation mask

Based on the initial segmentation result as described in the previous section, a local refinement is performed on the updated probability map to segment the remaining tumor tissue. Since an automatic identification of a volume-of-interest containing the tumor is difficult and would require additional processing steps, we use a region growing approach. Thereby, neighboring voxels are added to the initial region as long as certain inclusion conditions are met. In order to provide an interactive adjustment of the segmentation mask we use a *progressive region growing* approach that has been proposed before in the context of vascular system analysis.[22] Common growing algorithms perform a segmentation for an a priori fixed inclusion condition and have to be repeated until an appropriate result is found. The progressive approach avoids this limitation and a segmentation is performed for a whole threshold range in parallel.

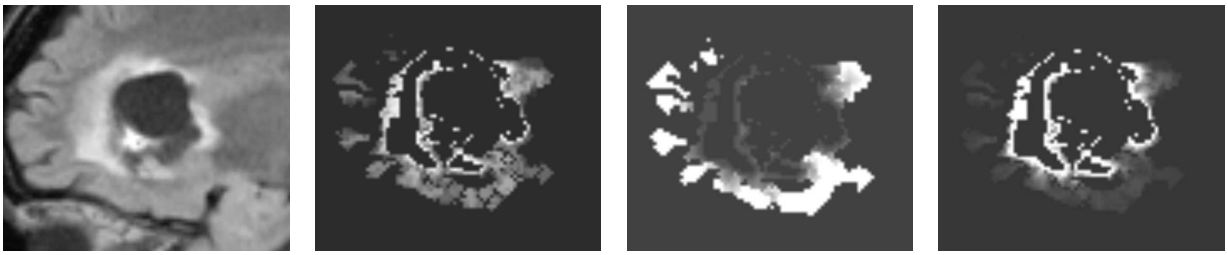

Figure 3. Comparison of segmentation thresholds applied to the tumor probability mask of a patient dataset. From left to right: Slice of patient dataset, probability threshold, distance threshold, and combination of probability and distance (quotient $r = v_p/\mathrm{dist}(v_p)$).

In a first step, a seed voxel set is computed from the boundary of the initial tumor segmentation result. Then, the 6 adjacent voxels (neighborhood N_6) are accumulated depending on a set of criteria. For an efficient implementation, a voxel list $\mathcal{L}$ is used to store the current lower probability threshold $\theta \in [\theta_{start}, \theta_{end}], \theta_{start} = 100$. The threshold is then decreased until a probability of $\theta_{end} = 0$ is reached. All evaluated voxels as well as the initially segmented voxels are labelled as visited. Our approach further extends the original progressive technique by means of different inclusion criteria and a final segmentation mask computation. Most important is the incorporation of an additional distance measure into the segmentation process that can be calculated on-the-fly in each accumulation step. This results in a geodesic distance transformation[23] starting from the initial tumor boundary. As described earlier, the initially computed probability map can have wrong values in both the tumor and non-tumor region (cf. Section 2.2.2). Our region growing method therefore also corrects the probability values for each considered voxel.

The applied criteria for voxel in- or exclusion are as follows: The first criterion is based on the probability threshold. High values in a low probability neighborhood are mostly due to noise and can be discarded. Therefore, voxels with $v_p > \theta$ result in an update of the probability, since these values should have already been accumulated in an earlier phase of the algorithm. We set $v_p := 0$ for small thresholds and $v_p := \theta$ otherwise. This also helps to avoid leakage of the tumor. All other voxels ($v_p \leq \theta$) are inserted into the currently considered list $\mathcal{L}(\theta)$. The second inclusion criterion provides a number of distance rules to the remaining voxels in the current list. To allow for a better differentiation of tumor voxels against adjacent non-tumor voxels, the current voxel distance is compared to the distance of neighboring voxels. A large distance plus a large distance difference to neighboring voxels can be considered as outlier, and the voxel is excluded ($v_p := \theta_{end}$) from the segmentation. On the other hand, voxels with a probability above a certain threshold and with a similar distance to the neighboring voxels are added to the tumor mask ($v_p := \theta_{start}$). A threshold of $v_p \geq 25$ has proven to be most appropriate.

The resulting region growing provides a new probability map plus a map with the corresponding distances. Both information can now also be used to compute the final tumor mask, in contrast to existing approaches that are typically based on the probability map alone. In this work, we combine the two values to compute the tumor mask, using the quotient $r = v_p/\text{dist}(v_p), r \in [\theta_{start}, \theta_{end}]$ for each voxel (cf. Fig. 3 (right)). This combination generally improves the probability for tumor close to the initial segmentation, and helps to avoid further leakage of the segmentation at positions with hardly visible tumor margins on an MR scan. Figure 3 shows a comparison of the three different segmentation thresholds, i.e. probability, distance, and the combination of both, applied to the tumor probability mask of an example patient dataset. An advantage of the combined measure for the considered segmentation task can be clearly observed.

3. RESULTS

The patient data used in this work were acquired on three different clinical 1.5T scanners (Siemens, Erlangen, Germany). The data-acquisition protocol contains sagittal T2- and FLAIR-weighted images as well as T1-weighted images after gadolinium MR contrast agent injection, all with an isotropic voxel size of 1.0mm^3, matrix 256×256, and about 160 slices. All datasets comprise primary brain tumors such as gliomas.

In this work, a 2D histogram feature space consisting of T2- and FLAIR-weighted images is utilized for the probabilistic tumor model generation as well as for the segmentation process. Considering only intensity values, this combination has shown to be the most appropriate choice. It enables a differentiation of tumor tissue from other tissue, e.g. cerebrospinal fluid, while the tumor region is hyperintense in both sequences. An utilization of FLAIR sequences alone on the other hand could impede the segmentation of cases where the tumor appears rather inhomogeneous on the MR images, and would thus require additional user interaction such as additional seed points.[5]

Currently, our histogram model is based on 29 patient datasets. A manual expert segmentation was performed for each dataset by outlining the tumor contours, in order to generate the actual tumor map. The model size has been fixed a priori to $\frac{2}{3}$ of the mean size of incorporated datasets, allowing for a faster registration. Thus, each patient data histogram has to be resampled to this size before registering. The resulting deformation field is then applied to the original histogram, requiring a resampling of the model.

The datasets were processed on an 2GHz AMD Athlon computer using the visual programming and rapid prototyping software platform MeVisLab.[24] The total execution time required for the segmentation method in the above mentioned fashion is approximately 10 minutes per case. Here, the pre-processing step is still the most time consuming part (motion correction: 4min, skull stripping: 3min). Especially the currently employed interactive skull stripping approach will be in the focus of further research in order to fully automatize this step. The initial tumor segmentation including the histogram model registration as well as the classification, transformation onto the image domain, and removement of isolated, mis-classified speckles, can be obtained in less than a minute. The final tumor segmentation can then be computed in about 30 seconds, mainly depending on the distance threshold used for the progressive region growing. The following interactive threshold adaptation typically does not require more than a few seconds.

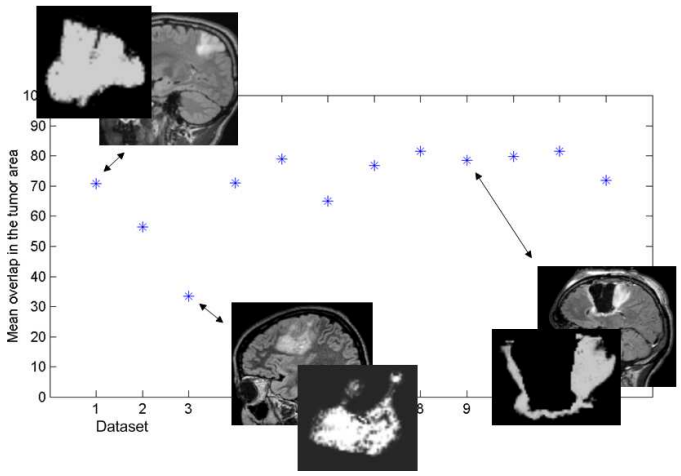

Figure 4. Accuracy and robustness of the employed global intensity feature. For different datapoints in the diagram, a slice of the corresponding patient dataset as well as the probability map for the tumor region is given.

3.1. Quality of proposed intensity feature

A transformation from the image domain into the histogram space as proposed in this work, results in a reduction of the original feature space. As mentioned above, combined global intensity values of the T2- and FLAIR-weighted images are selected. Here, we provide a statistical analysis of the accuracy and robustness of this feature. Therefore, expert segmentations are transformed into the histogram feature space, and then back into the image domain. We compute the sum of all resulting probability values within the tumor region to measure the quality of the intensity feature. An analysis is performed on 12 patient datasets, including different tumor shapes, sizes, and locations.

The mean value over all cases is 70.52 ± 13.87 (see also Fig. 4). This rather low value results from the transformation imposed data reduction. In this case, the transformation between image domain and histogram domain is not bijective, but merely surjective. An example could be given as follows: if 50 of 100 voxels with the same intensity are labeled as tumor in an image, the histogram tumor probability will be set to 50%. The inverse transformation back into the image domain will however result in 100 voxels labeled with 50%. Figure 4 shows the resulting tumor probability values, restricted to the area of the expert segmentation. Different datasets with large mean value as well as a dataset with a low mean mean value are presented.

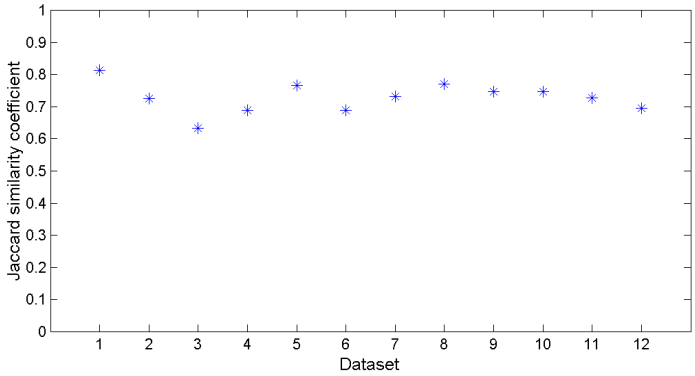

Figure 5. Analysis of the tumor segmentation accuracy with respect to a manual expert segmentation using the Jaccard similarity metric for different patient datasets.

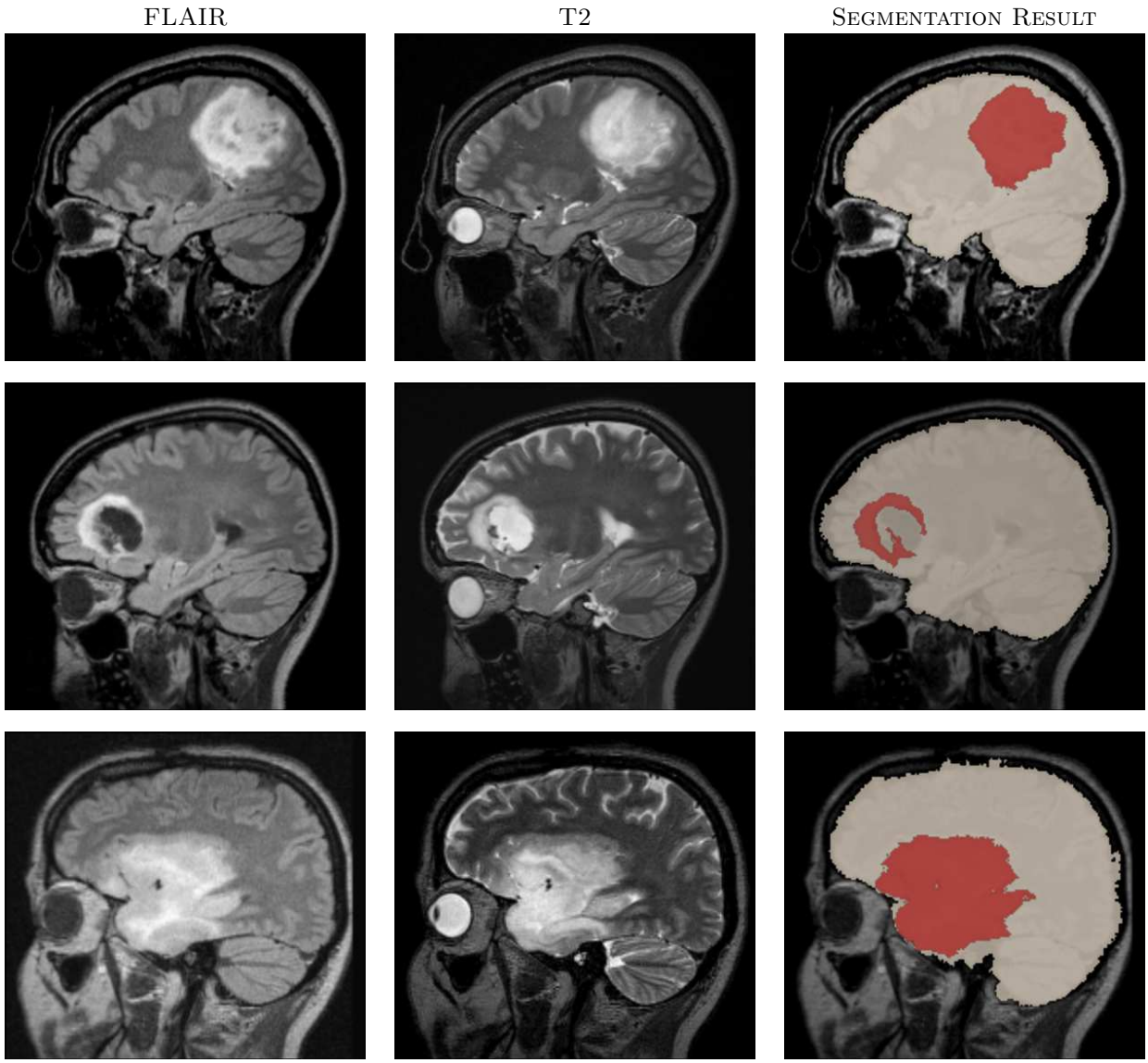

Figure 6. Segmentation results of different patient datasets. From left to right: Slice of FLAIR dataset, slice of T2 dataset, combined overlay of skull stripping and tumor segmentation result.

3.2. Segmentation results

The proposed segmentation method has been validated on 12 patient datasets, that were already used in the previous section. The reliability of our method is illustrated in Figure 5. The Jaccard similarity coefficient[25] $J = (A \cap B)/(A \cup B) \in [0, 1]$ is used to measure the overlap between manual expert segmentations and computed segmentation. The overall mean accuracy of the segmentation for all 12 cases is 0.73 ± 0.05. For visual inspection, segmentation results for different patient datasets are shown in Figure 6 and Figure 7. The results illustrate the potential of our approach.

4. DISCUSSION AND CONCLUSION

In this work we present a new approach for fast multispectral segmentation of brain tumors. A new, efficient initialization based on a probabilistic model of cross-subject intensity variability is proposed, created in a multispectral histogram space. A progressive region growing approach is used to compute a fast tumor segmentation.

Combined probability and distance information add to flexibility and precision. Especially no assumptions about the tumor shape are required in this approach, which represents an advantage in cases where the tumor shape is very irregular, or in the case of patient data acquired after surgical rescection. Furthermore, a statistical measure of accuracy and robustness of the selected histogram features for segmentation is proposed. Currently, 12 clinical datasets are used for evaluation. Future work will investigate the generalization of our approach to a variety of other sequences and MR scanners. Furthermore, we plan an automation of the currently remaining interactive steps, including the skull stripping and the final threshold adaptation.

REFERENCES

1. A. Osborn and K. Tong, *Handbook of Neuroradiology: Brain and Skull*, Mosby-Year Book, 1999 2nd edition.
2. B. Joe, M. Fukui, C. Meltzer, Q. Huang, R. Day, P. Greer, and M. Bozi, "Brain tumor volume measurement: Comparison of manual and semiautomated methods," *Radiology* **212**, pp. 811–816, 1999.
3. M. Clark, L. Hall, D. Goldgof, R. Velthuizen, F. Murtagh, and M. Silbiger, "Automatic Tumor Segmentation Using Knowledge-Based Techniques," *IEEE Trans Med Imag* **17**(2), pp. 187–201, 1998.
4. M. Prastawa, N. Moon, E. Bullitt, K. van Leemput, and G. Gerig, "Automatic brain and tumor segmentation," *Academic Radiology* **10**, pp. 1341–1348, Dec. 2003.
5. G. Moonis, J. Liu, J. Udupa, and D. Hackney, "Estimation of tumor volume with fuzzy-connectedness segmentation of mr images," *Am J Neuroradiol* **23**(3), pp. 356–63, 2002.
6. M.Kaus, S. Warfield, A. Nabavi, P. Black, F. Jolesz, and R. Kikinis, "Automated segmentation of mr images of brain tumors," *Radiology* **218**(2), pp. 586–91, 2001.
7. S. Warfield, M. Kaus, F. Jolesz, and R. Kikinis, "Adaptive, template moderated, spatially varying statistical classification," *Med Imag Anal* **4**, pp. 43–55, 2000.
8. S. Ho, E. Bullitt, and G. Gerig, "Level set evolution with region competition: Automatic 3-d segmentation of brain tumors," in *ICPR*, pp. 532–536, 2002.
9. M. Droske, M. Meyer, M. Rumpf, and C. Schaller, "An adaptive level set method for interactive segmentation of intracranial tumors," *Neurosurgical Research* **27**(4), pp. 363–370, 2005.
10. A. Popovic, T. Wu, M. Engelhardt, and K. Radermacher, "Modeling of intensity priors for knowledge-based level set algorithm in calvarial tumors segmentation," in *Proc. MICCAI*, pp. 864–871, 2006.
11. K. van Leemput, F. Maes, D. Vandermeulen, and P. Suetens, "Automated model-based tissue classification of mr images of the brain," *IEEE Trans Med Imag* **18**, pp. 897–908, 1999.
12. W. Touhami, D. Boukerroui, and J.-P. Cocquerez, "Fully automatic kidneys detection in 2d ct images: A statistical approach," in *Proc. MICCAI*, pp. 262–269, 2005.
13. D. Collins, A. Zijdenbos, V. Kollokian, J. Sled, N. Kabani, C. Holmes, and A. Evans, "Design and construction of a realistic digital brain phantom," *IEEE Trans Med Imaging* **17**(5), pp. 463–468, 1998.
14. A. Toga, P. Thompson, K. Narr, and E. Sowell, "Probabilistic brain atlases of normal and diseased populations," in *Databasing the Brain: From Data to Knowledge*, ch. 25, John Wiley & Sons, Inc., 2003.
15. T. Rohlfing, R. Brandt, R. Menzel, and C. Maurer, "Evaluation of atlas selection strategies for atlas-based image segmentation with application to confocal microscopy images of bee brains," *NeuroImage* **21**, pp. 1428–1442, 2004.
16. A. Wismueller, F. Vietze, J. Behrends, A. Meyer-Baese, M. Reiser, and H. Ritter, "Fully automated biomedical image segmentation by self-organized model adaptation," *Neural Networks* **17**(8), pp. 1327–1344, 2004.
17. F.Vega-Higuera, N. Sauber, B. Tomandl, C. Nimsky, G. Greiner, and P. Hastreiter, "Automatic adjustment of bidimensional transfer functions for direct volume visualization of intracranial aneurysms," in *Medical Imaging, Proc. SPIE*, pp. 275–284, 2004.
18. J. Weickert, *Anisotropic diffusion in image processing*, Teubner, 1997.
19. D. Rueckert, L. Sonoda, C. Hayes, D. Hill, M. Leach, and D. Hawkes, "Non-rigid registration using free-form deformations: Application to breast MR images," *IEEE Trans Med Imag* **18**(8), pp. 712–721, 1999.
20. J. Pluim, J. Maintz, and M. Viergever, "Mutual-information-based registration of medical images: a survey," *IEEE Trans Med Imag* **22**(8), pp. 986–1004, 2003.
21. H. Hahn and H.-O. Peitgen, "The skull stripping problem in mri solved by a single 3d watershed transform," in *Proc. MICCAI*, pp. 134–143, 2000.

22. T. Boskamp, H. Hahn, M. Hindennach, S. Oeltze, B. Preim, S. Zidowitz, and H. Peitgen, "Geometrical and structural analysis of vessel systems in 3d medical datasets," in *Medical Imaging Systems: Technology and Applications*, ch. 5, World Scientific Press, 2006.
23. P. Soille, *Morphological Image Analysis: Principles and Applications*, Springer, 2003.
24. MeVisLab 1.5, homepage at. `http://www.mevislab.de`.
25. P. Jaccard, "The distribution of flora in the alpine zone," *The New Phytologist* **11**(2), pp. 37–50, 1912.

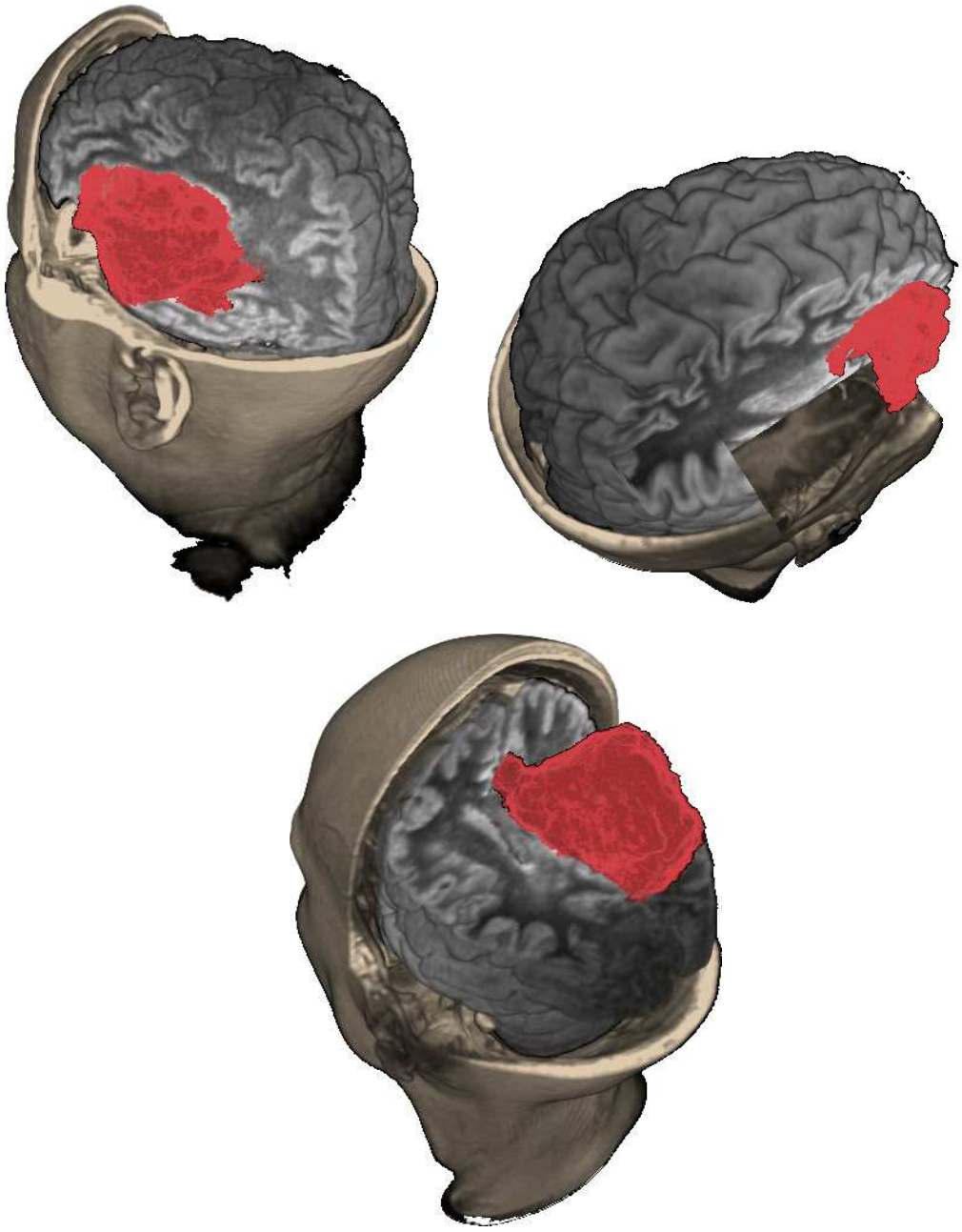

Figure 7. Segmentation results in 3D of the patient datasets shown in Figure 6.